Optimal Control Design of Preparation Pulses for Contrast Optimization in MRI

Eric Van Reeth[a], Hélène Ratiney[a], Michael Tesch[b], Denis Grenier[a], Olivier Beuf[a], Steffen J. Glaser[b], Dominique Sugny[c,d]

[a] *CREATIS, CNRS UMR5220 – INSERM U1206 – Université Lyon 1 – INSA Lyon - Université Jean Monnet Saint-Etienne, France*
[b] *Department of Chemistry, Technische Universität München, Germany*
[c] *ICB, CNRS UMR6303, Université de Bourgogne-Franche Comté, France*
[d] *Institute for Advanced Study, Technische Universität München, Lichtenbergstrasse 2a, D-85748 Garching, Germany*

Abstract

This work investigates the use of MRI radio-frequency (RF) pulses designed within the framework of optimal control theory for image contrast optimization. The magnetization evolution is modeled with Bloch equations, which defines a dynamic system that can be controlled via the application of the Pontryagin Maximum Principle (PMP). This framework allows the computation of optimal RF pulses that bring the magnetization to a given state to obtain the desired contrast after acquisition. Creating contrast through the optimal manipulation of Bloch equations is a new way of handling contrast in MRI, which can explore the theoretical limits of the system.
Simulation experiments carried out on-resonance quantify the contrast improvement when compared to standard T_1 or T_2 weighting strategies. The use of optimal pulses is also validated for the first time in both *in vitro* and *in vivo* experiments on a small-animal 4.7 T MR system. Results demonstrate their robustness to static field inhomogeneities as well as the fact that they can be embedded in standard imaging sequences without affecting standard parameters such as slice selection or echo type. *In vivo* results on rat and mouse brains illustrate the ability of optimal contrast pulses to create non-trivial contrasts on well-studied structures (white matter versus gray matter).

Keywords: Optimal control, RF pulses, contrast, Bloch equations

1. Introduction

Magnetic Resonance Imaging (MRI) is a widely used imaging modality for both clinical and pre-clinical studies, mainly due to the large variety of achievable contrasts. Well-contrasted images are desired to ensure the correct visualization of internal body structures, to allow accurate image reading and proper diagnosis.

Contrast in MRI originates from differences in intrinsic tissue properties such as proton density, relaxation times, chemical shift or proton motion [1]. Acquisition parameters such as echo time (TE), repetition time (TR) and flip angle (θ) are typically tuned to emphasize the tissue property differences and create various image weighting. Systematic acquisition strategies are often used to obtain the desired contrast which offers no guarantee about the contrast optimality. Typical T_2 weighted images are obtained by tuning TE in order to maximize the transverse magnetization difference. Typical T_1 weighting is achieved with inversion recovery (IR) strategies or by setting TR values well bellow T_1 values.

The objective of this work is to design radio-frequency (RF) pulses that create maximal contrast between species for which relaxation times are known. They associate the effects of magnetization relaxation and RF excitation to bring the magnetization to a state that will produce the desired contrast. Following the principles of optimal control theory, this approach has several advantages over typical contrast strategies: i) it pushes the obtained contrast towards its theoretical bound, ii) it can generate contrasts that cannot be obtained with classical acquisition strategies, iii) experimental inhomogeneities can be incorporated in the problem which makes this approach applicable in pre-clinical and clinical studies.

The use of optimal control for RF pulse design in MRI is not new. It has been investigated in the context of robust excitation and refocusing [2–12], parallel transmission [13–19], and contrast optimization [20–26]. The present paper builds upon the previous works on contrast optimization and proposes several advances: i) for the first time, quantitative comparison with standard T_1/T_2 weighting is performed on a large range of relaxation times to study configurations where optimal contrast pulses improve standard contrast ii) optimal control pulses are integrated into standard imaging sequences as preparation pulses that allow slice selectivity iii) *in vitro* experiments showing various contrast configurations are presented to validate the simulation experiments, and iv) the first *in vivo* acquisition using an optimal contrast

pulse is presented.
The paper is organized as follows. In the first section, the optimal control framework via the application of the Pontryagin Maximum Principle is described in the context of magnetization control in NMR [27]. Simulation results are then compared with standard contrast strategies. Later, both *in vitro* and *in vivo* results are presented to show the versatility of the proposed approach and to validate its use on a small-animal 4.7 T Bruker MR system.

2. Methods

2.1. Pontryagin Maximum Principle

The Pontryagin Maximum Principle (PMP) [28] is a powerful tool to solve optimal control problems. It allows the computation of a control function that optimizes the evolution of a given dynamic system, while minimizing a user-defined cost function. The PMP, in the present case of a Mayer problem [20], is based on the definition of a pseudo-Hamiltonian:

$$H = \overrightarrow{P}.\dot{\overrightarrow{M}} \tag{1}$$

in which $\overrightarrow{P}$ is the adjoint state vector which can be interpreted as the Lagrange multiplier associated with the state variable $\overrightarrow{M}$. In the current case, $\overrightarrow{M}$ represents the magnetization vector, whose evolution is governed by the Bloch equations:

$$\frac{d}{dt}\begin{pmatrix} M_x \\ M_y \\ M_z \end{pmatrix} = \begin{pmatrix} -\frac{1}{T_2} & \Delta_{B_0} & -\omega_y \\ -\Delta_{B_0} & -\frac{1}{T_2} & \omega_x \\ \omega_y & -\omega_x & -\frac{1}{T_1} \end{pmatrix}\begin{pmatrix} M_x \\ M_y \\ M_z \end{pmatrix} + \begin{pmatrix} 0 \\ 0 \\ \frac{M_0}{T_1} \end{pmatrix} \tag{2}$$

with Δ_{B_0} the resonance offset, M_0 the equilibrium magnetization and (ω_x, ω_y) respectively the x and y components (in the rotating frame of reference) of the RF pulse to be optimized.
The PMP states that the optimal control, $\boldsymbol{\omega}^\star = (\omega_x^\star, \omega_y^\star)$, the optimal state trajectory, $\overrightarrow{M}^\star$, and the associated adjoint state, $\overrightarrow{P}^\star$, must maximize the Hamiltonian during the whole control time:

$$H(\overrightarrow{M^\star}, \overrightarrow{P^\star}, \boldsymbol{\omega}^\star) = \max_{\boldsymbol{\omega}\in\Omega} H(\overrightarrow{M}, \overrightarrow{P}, \boldsymbol{\omega}) \tag{3}$$

where $\Omega \in \mathbb{R}$ is the set of admissible controls.
The optimal magnetization and adjoint trajectories then fulfill the Hamiltonian equations:

$$\dot{\overrightarrow{M}} = \frac{\partial H}{\partial \overrightarrow{P}} \quad ; \quad \dot{\overrightarrow{P}} = -\frac{\partial H}{\partial \overrightarrow{M}} \tag{4}$$

Finally, extremal trajectories must respect the transversality conditions [22], which in our case reduce to:

$$\overrightarrow{M}(t_0) = \begin{pmatrix} 0 \\ 0 \\ M_0 \end{pmatrix} \quad ; \quad \overrightarrow{P}(t_f) = -\frac{\partial C}{\partial \overrightarrow{M}}(\overrightarrow{M}(t_f)) \tag{5}$$

with C the cost function and $[t_0,\ t_f]$ the control time interval. The PMP, as stated here, defines a system of coupled equations with fixed boundary conditions at initial time for $\overrightarrow{M}$ and final time for $\overrightarrow{P}$, that can be solved either with geometric or numerical approaches. Geometric methods are however limited to low dimensional systems [20, 29], which limits their use for realistic MRI simulations. Fully numerical methods, such as Krotov [10] or gradient ascent approaches [30], are generally used to simultaneously control a larger number of spins.

2.2. The GRAPE Algorithm

The GRadient Ascent Pulse Engineering (GRAPE) algorithm is a gradient ascent (or descent) based algorithm initially introduced for Nuclear Magnetic Resonance optimal pulse design [30]. It aims at computing the optimal RF pulse and magnetization trajectories that fulfill the optimality conditions. Starting from an initial guess, the control field is iteratively updated to improve the cost function, while fulfilling the constraints imposed by the PMP. A basic version of the algorithm can be summarized in the following steps:

1. Choice of the initial control field $\boldsymbol{\omega}^{(0)}$
2. Forward temporal propagation of the magnetization state $\overrightarrow{M}(t)$ from the boundary condition: $\overrightarrow{M}(t_0)$ (following the Hamiltonian equations 4 and 5)
3. Backward temporal propagation of the adjoint state $\overrightarrow{P}(t)$ from the boundary condition: $\overrightarrow{P}(t_f)$ (following the Hamiltonian equations 4 and 5)

4. Update of the current control field from the previous estimation (following the maximization condition of Eq 3):

$$\boldsymbol{\omega}^{(k+1)} = \boldsymbol{\omega}^{(k)} - \alpha \frac{\partial C}{\partial \boldsymbol{\omega}}$$

with $\alpha > 0$.

5. Repeat steps 2 to 4 until convergence is reached

It is worth noticing that using a first order approximation, there is an equivalence between the relations ($\frac{\partial H}{\partial \boldsymbol{\omega}} = 0$) and ($\frac{\partial C}{\partial \boldsymbol{\omega}} = 0$), which justifies the computation of the cost function derivative at Step 4 to meet the maximization condition of Eq. 3.

Since the optimal contrast problem is tackled here with a purely numerical approach, the dynamic has to be discretized. The control time interval $[t_0, t_f]$ is equally divided into N steps of length Δt during which the control field $\boldsymbol{\omega}(t_k) = \boldsymbol{\omega}_{t_k}$ is assumed to be constant. The evolution operator U_{t_k} is defined such that $\overrightarrow{M}(t_k + dt) = U_{t_k}\overrightarrow{M}(t_k)$. As was proposed in the initial implementation [30], the gradient term ($\frac{\partial C}{\partial \boldsymbol{\omega}}$) is computed at each temporal step using the forward and backward propagation of respectively the magnetization and adjoint states:

$$\frac{\partial C}{\partial \boldsymbol{\omega}_{t_k}} = \overrightarrow{P}_{t_k} \frac{\partial U_{t_k}}{\partial \boldsymbol{\omega}_{t_k}} \overrightarrow{M}_{t_k}$$

where $\overrightarrow{P}_{t_k} = \overrightarrow{P}_{t_f} U_{t_f} \dots U_{t_{k+1}}$ and $\overrightarrow{M}_{t_k} = U_{t_{k-1}} \dots U_{t_1} \overrightarrow{M}_{t_0}$.

In the present implementation, the term $\frac{\partial U_{t_k}}{\partial \boldsymbol{\omega}_{t_k}}$ is approximated using complex differentiation as suggested in [31, 32]. The idea behind it is to express the Taylor series expansion of a function $f : \mathbb{R}^n \to \mathbb{R}$, to which is added a small complex increment:

$$f(x + ih) = f(x) + ihf'(x) - \frac{h^2}{2} f^{(2)}(x) + \dots$$

which leads to the following derivative formulation, by taking the imaginary part of both sides of the equation:

$$f'(x) \approx \frac{\mathrm{Im}\left(f(x + ih)\right)}{h}$$

This leads to the following gradient expression:

$$\frac{\partial C}{\partial \boldsymbol{\omega}_{t_k}} = \frac{1}{h} \mathrm{Im}\left(\overrightarrow{P}_{t_k} U_{t_k}(\omega_{t_k} + ih)\overrightarrow{M}_{t_k}\right) \tag{6}$$

Using Eq 6 as a derivative expression significantly reduces the approximation error when small values of h are used [32]. In subsequent simulations, h is set to 10^{-10}.

2.3. Cost Function

In the context of contrast optimization, the goal is to maximize the difference between the transverse magnetization of 2 samples with different relaxation times, but subjected to the same RF pulse. In this problem we consider that the global NMR signal is formed by the sum of the 2 magnetization contributions: $\overrightarrow{M}^{(a)} = \left(M_x^{(a)}\, M_y^{(a)}\, M_z^{(a)}\right)$ and $\overrightarrow{M}^{(b)} = \left(M_x^{(b)}\, M_y^{(b)}\, M_z^{(b)}\right)$. In the present study, optimal contrast is defined as the maximization of the transverse magnetization difference between both samples, at the end of the control time t_f. Let us consider the case where samples a and b are respectively maximized and minimized (denoted $(a > b)$ later on). The corresponding cost function can be expressed as:

$$C^{a>b} = \|\overrightarrow{M}_{\perp}^{(b)}(t_f)\| - M_x^{(a)}(t_f) \tag{7}$$

where $\overrightarrow{M}_{\perp} = (M_x,\, M_y)$ represents the transverse magnetization, i.e. the detectable NMR signal. This cost function decreases as $\overrightarrow{M}_{\perp}^{(b)}(t_f)$ tends to $(0,\, 0)$ and as $M_x^{(a)}(t_f)$ tends to 1. Forcing the magnetization of sample a to the positive x-axis controls the phase of the magnetization. This has no impact when only spins on resonance are considered, but it has to be considered in the presence of off-resonance effects (see section 4.2) to preserve intra-voxel phase coherence.

2.4. Implementation Details

Temporal discretization. The temporal sampling period is fixed around ($\Delta t \approx 150\mu s$) in following experiments. This was empirically found to be a good compromise, as there are no general rule to set it, between computational complexity and accurate representation of the magnetization evolution. It was chosen to be sufficiently small with respect to the variation of the RF coefficients, by making sure that the magnetization evolution is properly controlled both in simulation and during experiments. Note that additional constraints or tailored convergence strategies can be implemented to limit the high frequency components of the optimal pulse [33].

Algorithm details. Various convergence schemes can be used to improve the initial gradient descent approach. Our implementation is based on a L-BFGS scheme which approximates the Hessian matrix from the cost function derivative. This improves both convergence speed and accuracy as discussed in [34]. Convergence is considered reached when the gradient norm is below a threshold that depends on the experiment (typically below 10^{-8}).
Note also that a typical L_2 norm approximation is used to facilitate its derivative computation:

$$\|\overrightarrow{M}_{\perp}(t_f)\| \approx \sqrt{M_x^2(t_f) + M_y^2(t_f) + \epsilon} \tag{8}$$

with $\epsilon = 10^{-10}$. This has important implications in the convergence process since $\overrightarrow{M}_{\perp} = (0, 0)$ at equilibrium.
Finally, a well-known drawback of gradient-based approaches is their inability to avoid local minima, which makes them strongly dependent on the initialization. This issue is tackled by taking multiple random initializations and retaining the best solution. Initial pulses are built as a sum of a spline curves with random amplitudes.

3. Simulation Experiments

3.1. Experiment Set-up

The objective of this study is to compare the best contrast that one can obtain between 2 samples (a and b), with standard T_1 and T_2 weighting and with optimal contrast pulses. The following paragraph describes how the best contrasts are computed when standard weighting is used.
The best T_2 weighting contrast is achieved after the application of a $\pi/2$ excitation pulse, during the T_2 decay of the transverse magnetization. The maximum magnetization difference is reached at a time which corresponds to the optimal TE. Its expression can be derived analytically by zeroing the derivative of the difference between both exponential T_2 decay curves:

$$t_f = \frac{\ln(T_2^a/T_2^b)}{1/T_2^b - 1/T_2^a} \tag{9}$$

An example of T_2 decay curves, showing the best achievable T_2 contrast is illustrated in Figure 1a.
The best T_1 weighting contrast occurs after the application of an inversion π

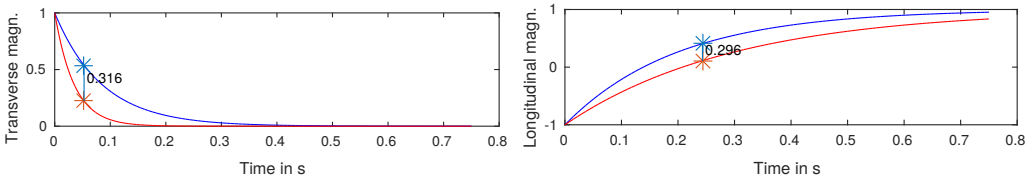

(a) Exponential T_2 decay after a $\pi/2$ excitation pulse

(b) Exponential T_1 recovery after a π inversion pulse

Figure 1: Illustration of best contrasts achievable with standard T_1 and T_2 weighting between sample a (blue): $[T_1^a, T_2^a] = [200, 85]$ ms, and sample b (red): $[T_1^b, T_2^b] = [300, 35]$ ms. The maximum magnetization differences obtained at $t_2^\star$ (a) and $t_1^\star$ (b) are also indicated.

pulse, during the T_1 recovery of the longitudinal magnetization. The maximum magnetization difference between the 2 samples is reached at a time usually called inversion time (TI), whose analytic expression can be computed in the same manner:

$$t_f = \frac{\ln(T_1^a/T_1^b)}{1/T_1^b - 1/T_1^a} \tag{10}$$

An example of T_1 recovery curves illustrating the best achievable contrast is shown in Figure 1b. Note that in the following, we assume that the magnetization on the longitudinal axis can be instantaneously transferred to the transverse plane with a $\pi/2$ pulse.

Optimal contrast results are computed in order to optimize the cost function given in Equation 7. The duration of the optimal pulses is set to 10% higher than the time that leads to the best T_1 contrast (Eq 10), in order to provide the RF pulse enough time to exploit both T_1 and T_2 relaxation time differences. Although shorter pulses could lead to similar results, RF pulses that do not require the whole control time are usually equal to 0 for a certain duration at the beginning of the pulse. In experiments, this approach does not seem to affect the contrast performance and significantly reduces the computation time.

Contrasts between samples a and b are computed for both methods on a wide range of T_2 values: $[T_2^a, T_2^b] \in [10, 200]$ ms. In order to reduce the number of numerical simulations, the T_1 values of both samples are fixed to: $T_1^a = 200$ ms and $T_1^b = 300$ ms. These values are purposely chosen so that the best contrast is balanced between T_1 and T_2 weighting. The contrast performance metric is defined as the opposite of the cost function defined in Eq. 7, that

was used to compute the optimal RF pulse:

$$\mathcal{P}^{a>b} = -\mathcal{C}^{a>b} = M_x^{(a)}(t_f) - \|\overrightarrow{M}_\perp^{(b)}(t_f)\| \tag{11}$$

Consequently, high values of $\mathcal{P}$ indicate that high contrasts are obtained.

3.2. Results

Let $\mathcal{P}_s$ and $\mathcal{P}_o$ respectively be the optimal contrast obtained with standard weighting and optimal control. Figure 2 illustrates the values taken by $\mathcal{P}_s^{a>b}$ and $\mathcal{P}_s^{b>a}$ on the considered T_2 range. It also shows the performance difference plots ($\mathcal{P}_o - \mathcal{P}_s$) in order to emphasize the contrast gain.
Standard weighting contrasts are displayed in Figures 2a and 2c. As could be expected, the results show that the best contrast is obtained when the T_2 value of the sample to be maximized (T_2^+) is significantly higher than the T_2 of sample to be minimized (T_2^-). When this difference decreases, the maximum contrast logically decreases. In regions where T_2 differences are small, or when ($T_2^- > T_2^+$), T_1 weighting obtained with inversion recovery strategy leads to better contrast. Comparing standard weighting curves also shows that in regions where T_1 contrast is better (flat regions), we have $\mathcal{P}_s^{a>b} > \mathcal{P}_s^{b>a}$. This is explained by the fact that $T_1^b > T_1^a$, which leads to a better inversion recovery situation when sample a is to be maximized.
Contrast results obtained with optimal control pulses are shown in Figures 2b and 2d. Three distinct regions can be distinguished. In regions close to the diagonal, i.e. when both T_2 values are close, T_1 contrast is predominant and there is no noticeable difference between standard weighting and optimal contrast. In these situations, optimal contrast pulses converge toward inversion recovery pulses to produce the desired contrast. An example of such pulse is given in Figure 3a, where a is to be maximized, ($[T_1^a, T_2^a]$ = [200, 80] ms) and ($[T_1^b, T_2^b]$ = [300, 105] ms). This figure also shows the simulated magnetization trajectories for both samples. T_1 contrast is clearly predominant here and the optimal pulse is close to a classic inversion recovery pulse. Here, both contrast performance metrics are equal to: $\mathcal{P}_o^{a>b} = \mathcal{P}_s^{a>b} = 0.29$.
In regions where T_2^+ is significantly higher than T_2^-, the effect of T_2 differences becomes predominant. It can however be noticed that optimal pulses are also able to take advantage of the T_1 differences to improve the obtained contrast by approximatively 10 %. An example of such situation is shown in Figure 3b where ($[T_1^a, T_2^a]$ = [200, 200] ms) and ($[T_1^b, T_2^b]$ = [300, 10] ms). In this situation, standard T_2 weighting leads to a contrast of $\mathcal{P}_s^{a>b} = 0.81$, while

optimal contrast reaches $\mathcal{P}_o^{a>b} = 0.92$. Analyzing the magnetization trajectories shows that the optimal RF pulse slowly brings sample b to saturation before flipping the residual magnetization of sample a into the transverse plane.
The last region of interest is the area where T_2^+ is lower than T_2^-. Here, optimal pulses are able to take advantage of the differences in T_2 to maximize the sample with the lowest T_2 value, which cannot be achieved with standard weighting. Such an example is shown in Figure 3c, where ($[T_1^a, T_2^a] = [200, 45]$ ms) and ($[T_1^b, T_2^b] = [300, 135]$ ms). Contrast metrics for these relaxation times are $\mathcal{P}_s^{a>b} = 0.29$ (T_1 contrast) and $\mathcal{P}_o^{a>b} = 0.44$, showing a clear impact of taking advantage of the differences in T_2. Analyzing the magnetization trajectories shows that the optimal pulse first slowly transfers the magnetization into the transverse plane. As sample a has lower T_1 and T_2 values, it reaches the longitudinal axis with a significant amount of magnetization while sample b almost reaches saturation. A final $\pi/2$ pulse flips the achieved longitudinal contrast into the transverse plane.

3.3. Interpretation

These results show that optimal pulses are able to combine the excitation process with T_1 and T_2 differences to create the optimal contrast between 2 samples. It is remarkable to notice that they converge towards standard weighting in obvious situations e.g. towards inversion recovery pulses when T_1 differences are predominant. But it is also interesting to note that it can create contrasts based on T_2 differences which cannot be exploited with regular weighting, i.e. when $T_2^+ < T_2^-$.
It can be expected that the evolution of the contrast performance is smooth with respect to small relaxation time variations. The fact that the contrast surface plots of Fig. 2b and 2d are indeed smooth, and the ability of optimal RF pulses to converge towards intuitive solutions in obvious contrast configurations suggest that the returned solutions are reasonably close to the global minima.
Optimal contrast curves can be plotted for any relaxation values in order to give insights about the best achievable contrast, infer the best acquisition strategy, and perhaps the need for contrast agents.
Moreover, it was noted that in order to maximize the contrast, the sample to be minimized is often saturated. Similar results were already noticed by Bonnard et al. in [29] when studying optimal contrast in minimal time using a geometrical approach. In addition, the convergence process mostly

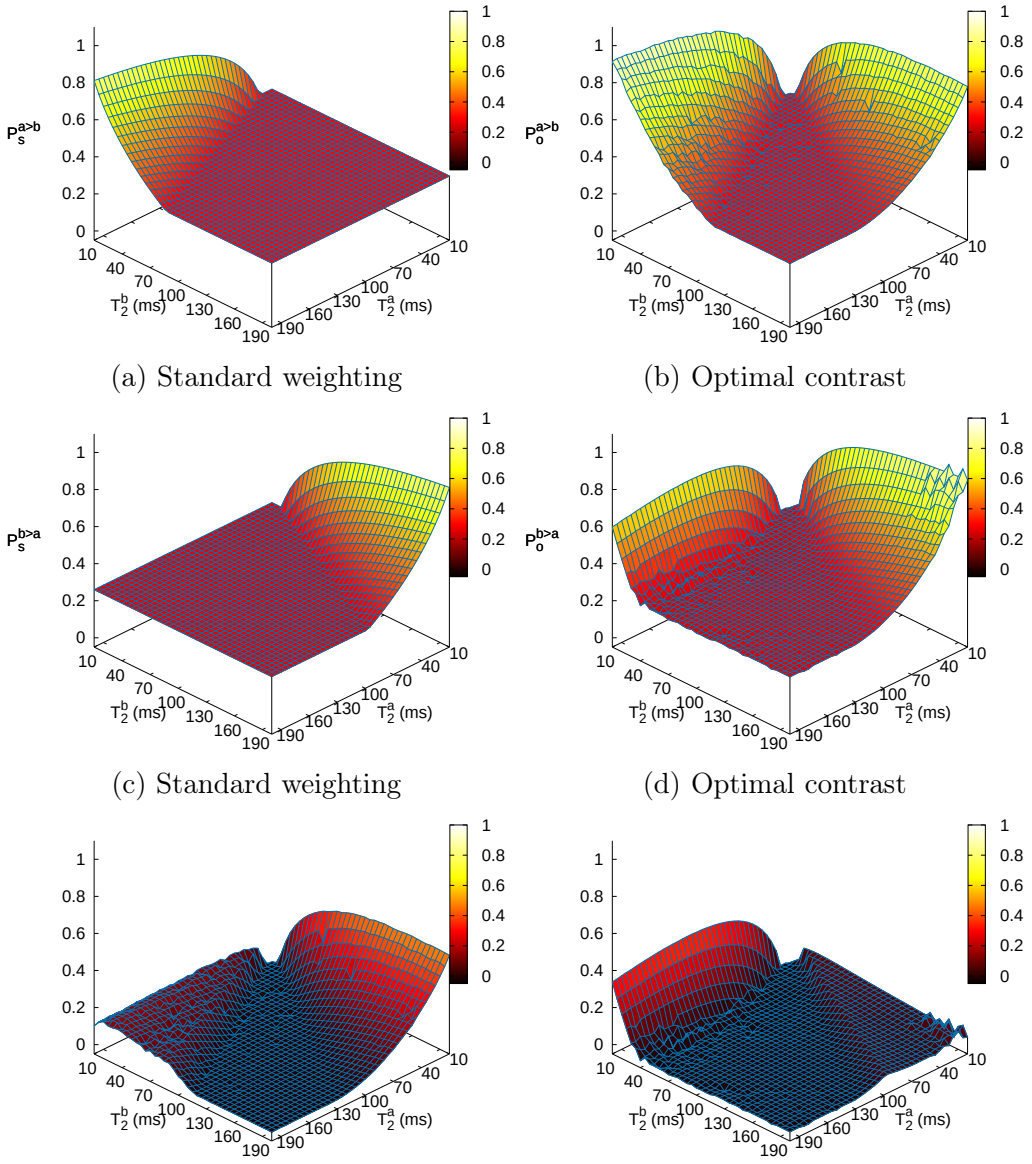

(a) Standard weighting

(b) Optimal contrast

(c) Standard weighting

(d) Optimal contrast

(e) Diff. plot: $\mathcal{P}_o^{a>b} - \mathcal{P}_s^{a>b}$

(f) Diff. plot: $\mathcal{P}_o^{b>a} - \mathcal{P}_s^{b>a}$

Figure 2: Comparison of best contrasts that can be obtained between 2 samples a ($T_1^a = 200$ ms) and b ($T_1^b = 300$ ms) using standard T_1 and T_2 weighting (a) and (d), optimal contrast pulses (b) and (d). First row: contrast configuration where a is maximized and b is minimized. Second row: contrast configuration where b is maximized and a is minimized. Last row: difference plots to emphasize the contrast gain.

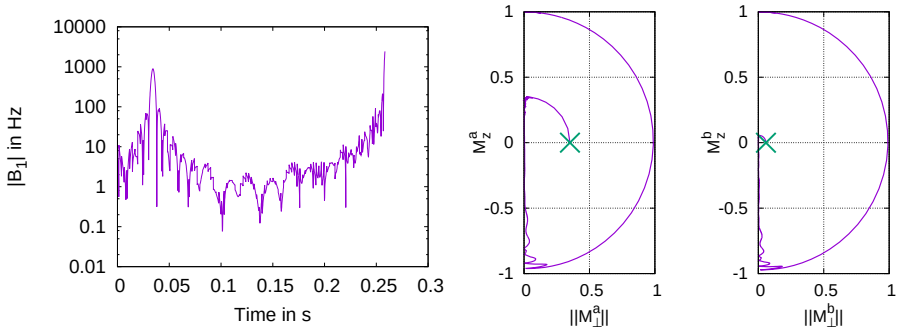

(a) $[T_1^a, T_2^a, T_1^b, T_2^b] = [200, 80, 300, 105]$ ms. Maximum RF amplitude is 2433 Hz.

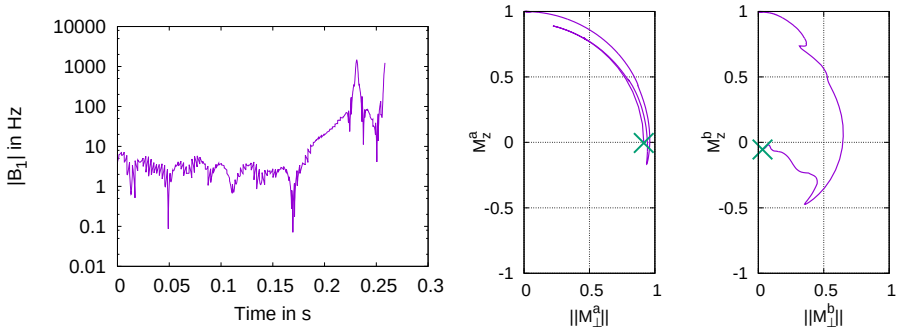

(b) $[T_1^a, T_2^a, T_1^b, T_2^b] = [200, 200, 300, 10]$ ms. Maximum RF amplitude is 1450 Hz.

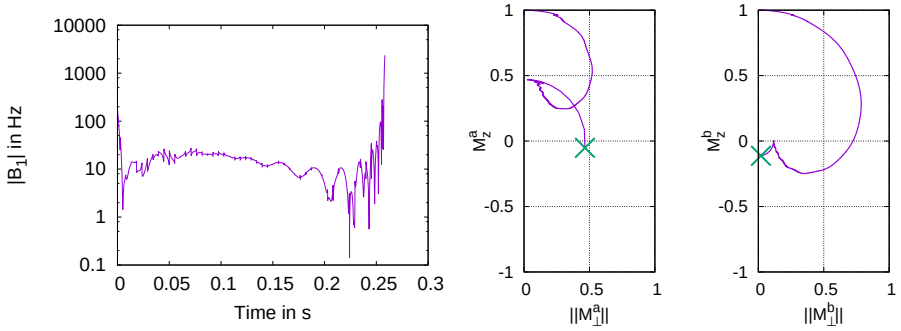

(c) $[T_1^a, T_2^a, T_1^b, T_2^b] = [200, 45, 300, 135]$ ms. Maximum RF amplitude is 2365 Hz.

Figure 3: Optimal pulses and magnetization trajectories in the Bloch sphere for various contrast configurations. Left: amplitude of the optimal RF pulse (on a log scale). Middle: trajectory of sample a. Right: trajectory of sample b.

Sample	1	2	3	4
T_1 (ms)	294	302	224	218
T_2 (ms)	70	40	67	38

Table 1: Relaxation times of the contrast phantom

struggled in transition regions where the optimal theoretical contrast shifts from T_2 to T_1, or vice versa. This corresponds to unstable regions where a slight variation in the dynamic model (e.g. slight change in the relaxation times) implies a large modification of the control function shape. In these situations, a careful initialization of the convergence process is key.

4. In Vitro Experiments

In this section, different contrast configurations are tested on a phantom composed of 4 samples for which resonance frequencies and proton densities are considered identical, but with different relaxation times. Samples were made with various concentrations of nickel sulfate, glycerol and distilled water. T_1 and T_2 relaxation times are adjusted by respectively changing the concentration of nickel sulfate and glycerol. Resulting relaxation time values are given in Table 1. They are measured using an exponential fit of the water peak acquired with a localized PRESS spectroscopy sequence for different TE and TR. All 4 samples are immersed and sealed into a cylinder filled with agar gel to reduce magnetic susceptibility artifacts. It also avoids air bubbles from forming, several weeks after the phantom is built. Acquisitions are carried out on a small animal 4.7T Bruker MR system using a 40 mm quadrature mouse body coil. In this practical experiment, the computation of RF pulses must take into consideration experimental variations and the integration into imaging sequences, which are detailed in subsequent sections.

4.1. Slice Selectivity

Optimal contrast pulse are designed as non-selective pulses which are applied before the excitation. This implies that the contrast is prepared on the z-axis as a preparation step, followed by standard slice-selective $\pi/2$ excitation schemes. The cost function defined is changed accordingly:

$$C_z^{a>b} = |M_z^{(b)}(t_f)| - M_z^{(a)}(t_f) \tag{12}$$

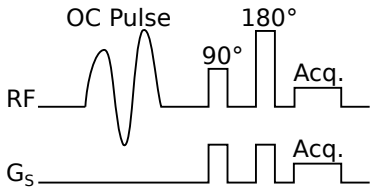

Figure 4: RF and slice-selection gradient sequence of a spin-echo acquisition with an optimal control pulse used as a contrast preparation step.

This strategy does not impact the final contrast performance since a simple $\pi/2$ pulse can switch the magnetization between the x-axis and the z-axis. An example of a spin echo sequence with contrast preparation is shown in Figure 4. Note that usual sequence improvements such as RARE acceleration [35] or multi-slice multi-echo schemes can be used, as long as TE is set as short as possible to preserve the prepared contrast.

4.2. Robustness to B_0 inhomogeneities

In real applications, the static B_0 magnetic field deviates from its nominal value due to both magnet imperfections and magnetic susceptibility of the object to be imaged. This produces significant resonance offsets which results in different magnetization trajectories for the same experienced RF field. Accurate magnetization control thus requires B_0-robust RF pulses, that leads all trajectories included in a given resonance offset range to the same magnetization state. This is done by discretizing an interval of B_0 offset values $[B_0^{min}\ ,\ B_0^{max}]$ in N_{B_0} values, each of them corresponding to a specific trajectory. The cost function given in Eq. 12 is thus adapted to consider all offsets:

$$C_z^{a>b} = \frac{1}{N_{B_0}} \left(\sum_{i=1}^{N_{B_0}} \left| M_z^{(b_i)}(t_f) \right| - M_z^{(a_i)}(t_f) \right) \tag{13}$$

This cost function imposes that $M_z^{(a_i)}(t_f)$ lies on the positive part of the z-axis. This might over-constrain the problem because it only affects the phase of the flipped signal, which does not impact the resulting contrast as long as intra-voxel coherence is kept. However, ensuring intra-voxel phase coherence imposes broadband constraints that depend on spatial resolution parameters and field map distribution, which might not been known in advance. For this reason, the generic cost function defined in Eq. 13 is used to guarantee phase coherence for all resonance offsets.

An illustration of a B_0-robust control is shown in Figure 5a using an inhomogeneity range of $[-30, 30]$ Hz, to generate the optimal contrast between samples 1 and 4. In practice, the robustness range is set in order to include both lower and upper bounds of the B_0 field map shown in Figure 6g. If the robustness range is too small, severe artifacts appear in the image. An illustration of such artifacts is shown in Figure 6f, where the robustness range is restricted to $[-10, 10]$ Hz. The circular patterns observed in this figure are typical magnetic susceptibility artifacts created by the interfaces between the phantom components. For all following *in vitro* experiments, the robustness range is set to $[-185, 185]$ Hz, which leads to far better results as can be seen in Figure 6c, for the same desired contrast.
Figure 5b illustrates the evolution of the cost function value with respect to the B_0 robustness range. A slight performance drop (around 9%) is observed when going from resonance to an inhomogeneous range: taking into account B_0 variations forces a change in the RF shape that slightly affects the resulting contrast. However, a similar level of performance is maintained until a significant robustness range (350 Hz) is reached. Although there is no guarantee that this behavior can be strictly generalized to all pulses, similar trends were observed in most experiments.
The frequency increment in this range is set to 5 Hz, which in turn sets the total number of considered trajectories N_{B_0}. There are no theoretical framework that can be used to set this increment value. It is thus chosen empirically by making sure that the evolution between two successive trajectories is smooth.

4.3. Results

The phantom configuration is shown in Figure 6a. The experiment consists in creating contrast between sample 1 (maximize) and the three other samples in three distinct acquisitions. The sequence used for the acquisition of optimal contrast images is a spin-echo sequence illustrated in Figure 4, with TR = 5 s, TE = 8 ms, slice thickness: 2 mm, matrix acquisition size: 128×128 with slice selective hermite excitation and refocusing pulses. The sequence used for the acquisition of regular contrast images is also a spin-echo sequence with similar parameters except for the TE which is set to optimize the desired contrast.
It is possible to quantify the amount of contrast generated by the different

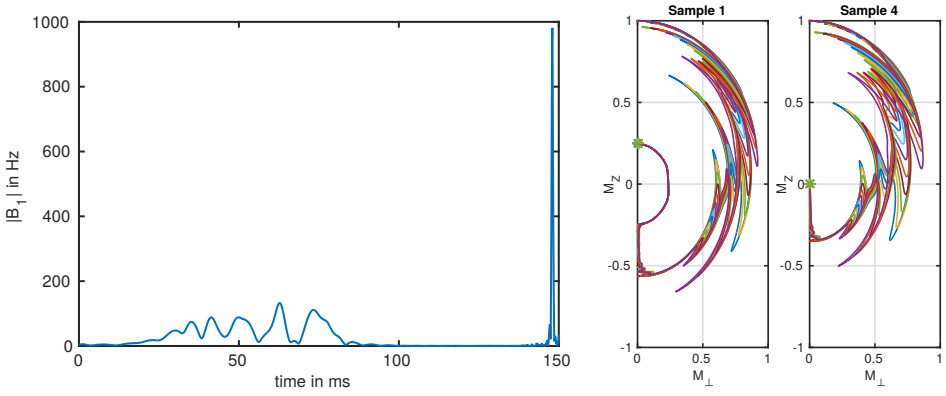

(a)

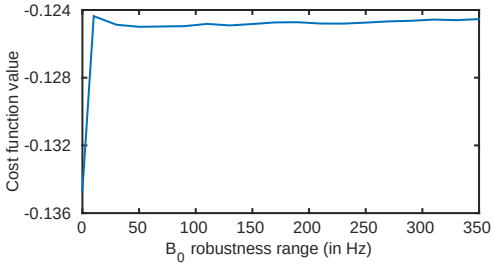

(b)

Figure 5: (a) Optimal RF pulse amplitude (left) and magnetization trajectories of both samples. Each trajectory represents a specific resonance offset in the interval $[-30, 30]$ Hz. (b) Evolution of the cost function value with respect to the B_0 robustness range.

acquisitions by computing the following metric:

$$\mathcal{Q}^{a,b} = \frac{I_a - I_b}{I_a}$$

with I_i corresponding to the average intensity of a given neighborhood fully contained in sample i.

The first experiment contrasts samples 1 and 2. Since their T_1 values are almost identical, contrast is mostly created by the T_2 differences. Two methods are compared: i) regular T_2 weighting is performed by setting the TE to its optimal value (52.2 ms), i.e. in order to optimize the transverse magnetization difference between both samples, and ii) optimal contrast acquisition obtained with the proposed optimal control design. Results are respectively shown in Figures 6b and 6c. The corresponding metric values were: $\mathcal{Q}_s^{1,2} = 0.31$ and $\mathcal{Q}_o^{1,2} = 0.33$, showing that the optimal pulse converges toward a pulse close to the standard T_2 weighting strategy. This result was already noticed in the simulation section where no resonance offsets were considered. It is interesting to notice that taking into account the B_0 variations did not degrade the initial optimal contrast.

The second experiment contrasts samples 1 and 3. In this case, contrast is based on T_1 differences since both T_2 values are almost equal. The result is shown in Figure 6d. As expected, an inversion recovery is performed, making sample 3 reach saturation before flipping the residual magnetization of sample 1 in the transverse plane with a $\pi/2$ pulse. In this experiment, the contrast metric is $\mathcal{Q}_o^{1,3} = 0.70$.

The last experiment contrasts samples 1 and 4. Here, both T_1 and T_2 values significantly differ. In this situation, the best standard weighting is theoretically based on T_2 differences for TE = 50.7 ms, which created an image almost identical to Figure 6b and a contrast metric of $\mathcal{Q}_s^{1,4} = 0.27$. As was observed in the simulation section, optimal pulses are able to benefit from both T_1 and T_2 differences to improve the standard contrast. A similar observation could be made in the *in vitro* experiment shown in Figure 6e. The corresponding metric value improved from: $\mathcal{Q}_s^{1,4} = 0.27$ to: $\mathcal{Q}_o^{1,4} = 0.42$, which validates the benefit of using optimal contrast pulses in practical applications.

In sequences using optimal contrast pulses, TE should be ideally set to 0 to avoid post-preparation T_2 relaxation that could deteriorate the prepared contrast. However, results suggest that for the range of considered T_2 values, setting TE to relatively small values (8 ms in our case) has little impact on the created contrast and preserves the prepared magnetization configuration.

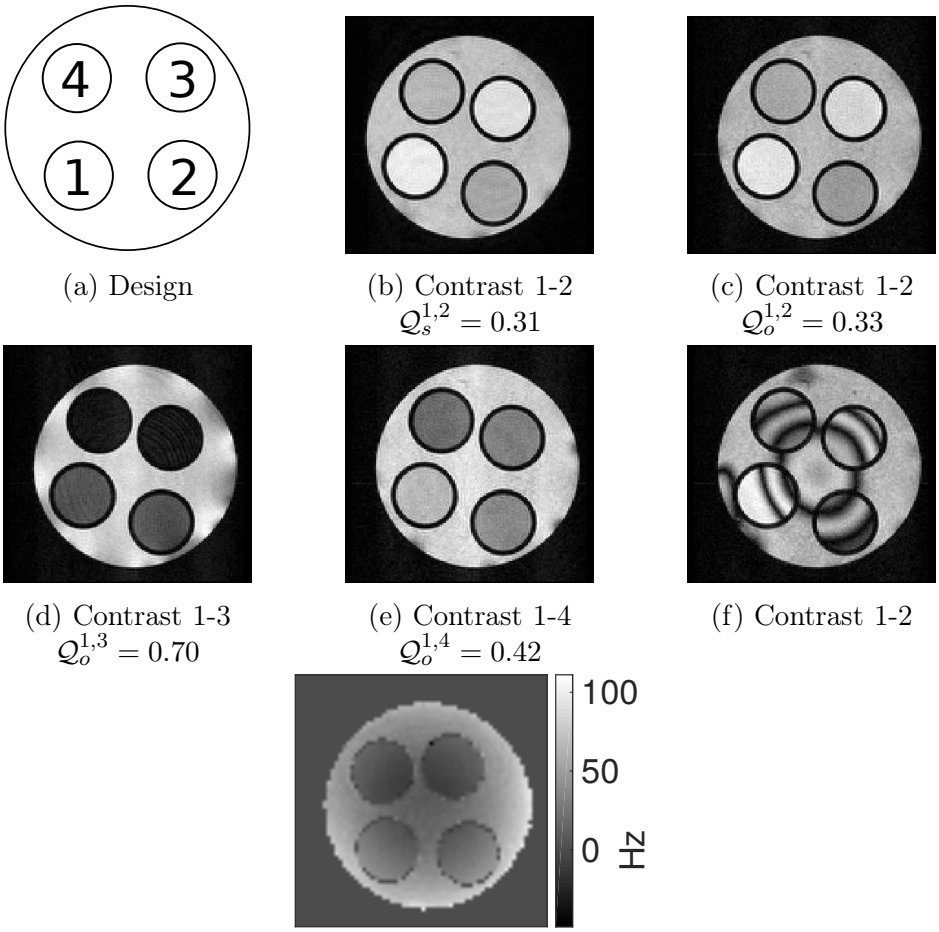

(a) Design

(b) Contrast 1-2 $\mathcal{Q}_s^{1,2} = 0.31$

(c) Contrast 1-2 $\mathcal{Q}_o^{1,2} = 0.33$

(d) Contrast 1-3 $\mathcal{Q}_o^{1,3} = 0.70$

(e) Contrast 1-4 $\mathcal{Q}_o^{1,4} = 0.42$

(f) Contrast 1-2

(g) Field map in Hz

Figure 6: *In vitro* experiment results. (a) Schematic representation of the phantom (b) Regular T_2 contrast at optimal TE (c)-(e) Contrast using optimal contrast pulses (f) Contrast using optimal contrast pulse when the B_0 robustness range is decreased to $[-10, 10]$ Hz (g) Field map in Hz acquired at the same slice position.

	Mouse Brain	Mouse Muscle	Rat Brain	Rat Muscle
T_1 (ms)	1062	1200	920	1011
T_2 (ms)	52	29	66	30

Table 2: Relaxation times estimation for the *in vivo* experiments

5. In Vivo Experiment

As an *in vivo* proof-of-concept, optimal contrast pulses were applied to an adult SWISS female mouse brain, and an adult female rat brain. Experiments were performed in accordance with the rules and regulations of the UCBL Ethic's Committee on animal experimentation. Prior to the examination, animals were kept on a 12 hours day/night rhythm in a 300 cm^2 plastic cage with straw bedding, pellet food and tap water. They were anesthetized using an isoflurane tabletop station (TEM Sega®, Lormont, France). The animal respiratory index was monitored during the experimentation using a pressure sensor placed on the chest. Acquisitions are carried out on the same small animal 4.7 T Bruker MR system using a 30 mm quadrature coil for the mouse experiment, and a 70 mm volumetric excitation coil together with a surface reception coil for the rat experiment. The average relaxation times of the targeted tissues were estimated with an exponential fit of the water peak acquired with a localized PRESS spectroscopy sequence for different TE (from 15 ms to 200 ms) and TR (from 500 ms to 7000 ms).
In order to illustrate the flexibility of optimal contrast pulses, a RF pulse is computed to optimize the contrast between the brain (minimize) and its surrounding parietal muscles (maximize). This contrast is chosen because it is challenging to obtain with standard contrast strategies for 2 main reasons: i) both T_1 values are close, which rules out inversion-recovery strategies, and ii) the T_2 of the muscle is shorter than the T_2 of the brain. Estimated relaxation times are given in Table 2. Referring to section 3, this corresponds to regions where $\mathcal{P}_o \gg \mathcal{P}_s$ in Figures 2e and 2f.
Pulses are designed to be B_0-robust for a range of $[-1\,,\,1]$ kHz for both experiments. Computation times required to design the corresponding optimal contrast pulses clearly depend on the B_0 robustness range considered, and the temporal discretization step. Running the proposed parallelized algorithm on a 8×2.7 GHz machine using Matlab (The MathWorks, Inc., Natick, MA, USA, R2015a) takes from a minute on resonance, up to around 20 hours for

an inhomogeneity range of $[-1, 1]$ kHz. Note that the pulse is computed only once for a given combination of relaxation times, and can be subsequently integrated into an imaging sequence without additional complexity. The amplitude of the computed optimal pulse for the mouse experiment is shown in Figure 7a, together with simulated magnetization trajectories corresponding to the brain and the parietal muscle. Each trajectory corresponds to a specific resonance frequency offset. It is worth noticing that despite the large disparity of magnetization trajectories when large frequency offsets are considered, the optimal pulse brings them all to the same state at the end of the control time (within a user-defined tolerance).

For the mouse experiment, a RARE sequence is used with an acceleration factor of 8, a centric encoding scheme, a matrix size of 192×192, TR = 5 s, TE = 9.4 ms and a slice thickness of 1.25 mm. Notice that TR has to be set long enough to ensure total longitudinal magnetization recovery. This condition is required by the current implementation of the optimal control algorithm, which requires the equilibrium to be the unique initial condition of the dynamic system. Acquisitions are shown in Figure 7b and 7c. Figure 7b shows the image obtained with the described RARE sequence when no contrast preparation pulse is used. Because of the long TR and short TE, relaxation times have no effect and the image intensity is mostly due to the proton density. On the other hand, Figure 7c shows the image obtained when the optimal preparation pulse is added, using the exact same sequence parameters. As expected, clear saturation of the brain is achieved while significant signal comes from the surrounding parietal muscles. It is also possible to distinguish the cerebrospinal fluid (CSF) which appears as a bright spot in the middle of the brain. This is due to its relaxation time values that are much higher than the other brain structures. It is also interesting to notice that the contrast is preserved in the whole slice, despite the proximity to the ear channels which create substantial field inhomogeneities due to air-tissue interfaces. This validates the choice of the B_0 robustness range. In this experiment, the average power deposition and peak power amplitude were respectively estimated to 0.53 Watts and 88 Watts. This corresponded to an attenuation of 15.1 dB, which lies well within reasonable bounds for *in vivo* acquisitions.

The rat acquisition is shown in Figure 7d, where a similar contrast as the mouse experiment can be observed. The same RARE sequence is used, with a matrix size of 128×128, TE = 8.8 ms, TR = 5 s and a slice thickness of 1.5 mm. However, although most of the brain is saturated, several internal

structures can be distinguished. For instance, Figure 7e shows the corpus callosum, the largest white matter structure, which appears brighter than its surrounding structures (mostly gray matter). This can be explained by the fact that relaxation times were estimated inside a voxel that was moslty composed of gray matter, which has a T_2 slightly longer than white matter (65ms versus 59ms at 4T) [36]. Figure 8 illustrates the simulated final signal map, i.e. the amount of signal left on the M_z axis after the optimal preparation pulse and before the excitation scheme, with respect to T_1 and T_2. This plot shows that the signal coming from short T_2 tissues is maximized, which explains why white matter appear slightly brighter than gray matter. It also shows that the pulse mainly uses T_2 differences to enhance short T_2 tissues, which is not trivial to obtain with standard contrast strategies. This particular contrast could open interesting perspectives in neuroimaging to optimize the discrimination between white and gray matter, which is key in actual clinical challenges such as the effect of aging or Alzheimer disease [37].

6. Discussion

Optimal pulses are computed based on the propagation of the Bloch equations which implies that prior information must be known both on the tissue to be imaged and on the imager itself. Relaxation times can be obtained with relative accuracy either by acquiring T_1 and T_2 maps, or by taking standard values from the literature. It is essential that the resulting contrast is robust to relaxation times estimation errors or inter-subjects variations. Figure 8 illustrates the smooth variation of the resulting longitudinal magnetization for the rat muscle/brain contrast, suggesting that the contrast is robust to reasonable relaxation times perturbations.
In presence of pathological tissues where nominal relaxation times are changed, optimal contrast pulses could be used as filters in the relaxation times space. A library of pulses can be generated to obtain a given contrast for healthy tissues. Any deviation from the expected contrast would imply significant changes in the tissues relaxation times, and thus a chance of pathology.
A reliable estimation of B_0 inhomogeneities must also be known, which can be obtained with reasonable accuracy by acquiring B_0 field maps. Both *in vitro* and *in vivo* studies have validated the pulse robustness to B_0 inhomogeneities which is key to the application of optimal contrast pulses to high-field MRI (e.g. 7 T) where field inhomogeneities are much higher. Note also that a

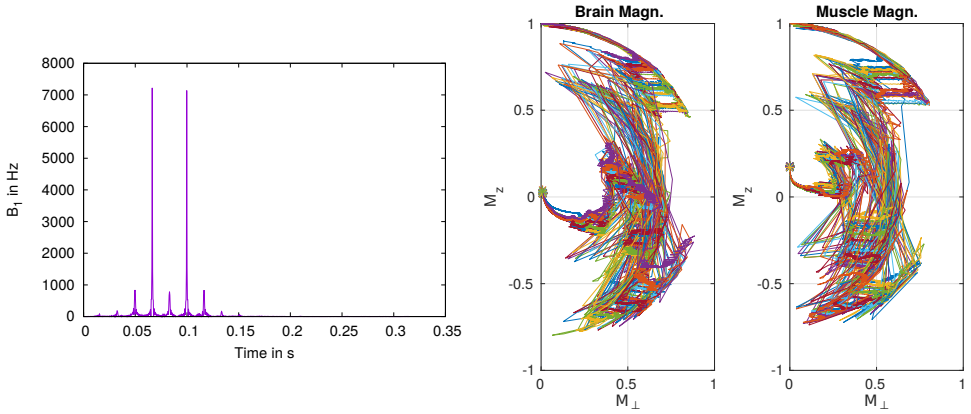

(a) RF amplitude and simulated trajectories computed for the mouse experiment. Each trajectory represents a specific resonance frequency offset.

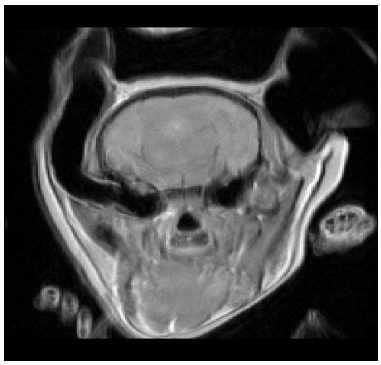

(b) Mouse acquisition without contrast preparation

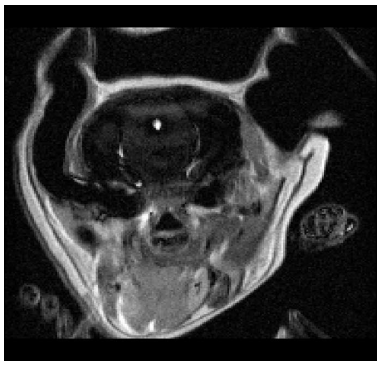

(c) Mouse acquisition with optimal contrast preparation

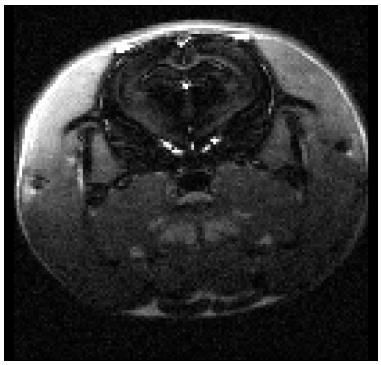

(d) Rat acquisition with optimal contrast preparation

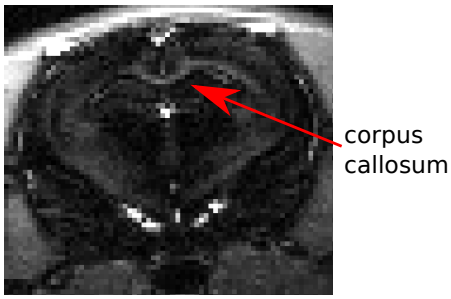

(e) Zoom on the corpus callosum region

Figure 7: *In vivo* contrast experiments on mouse and rat brains consisting of saturating the brain while maximizing the signal coming from the outer muscles

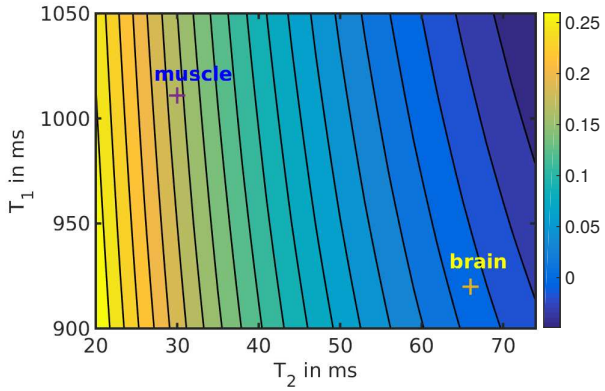

Figure 8: Resulting longitudinal magnetization (M_z) after the application of the optimal pulse for the rat muscle/brain contrast. The smoothness of the evolution illustrates the pulse robustness to small relaxation times estimation errors.

similar robustness approach can be used for T_1 and T_2 deviations as well as B_1 variations to account for the coil inhomogeneity excitation profile [21]. This would be an important parameter for applications using surface coils for excitation.

In this work, only relaxation time differences were used to create contrast between 2 samples. Other sources of contrast such as chemical shift, proton density differences or any other parameter that influences the magnetization trajectory could also be used without any change in the present optimization framework. This would surely improve the best achievable contrast and boost the impact of optimal contrast pulses for applications such as water/fat contrast imaging or spectroscopy.

The integration strategy of optimal contrast pulses into imaging sequences was to use them as preparation pulses. This makes the choice of the image contrast independent of the excitation scheme (gradient-echo or spin-echo), and enables the use of standard excitation pulses.

Power requirement of optimal contrast pulses is usually not an issue for three main reasons: i) the pulse duration usually contains long periods during which the B_1 amplitude is null in order to let relaxation occur, which results in a very low average power deposition (few Watts), and ii) maximum peak power can be bounded to limit the energy deposition. An additional penalization term can also be added in the cost function to penalize high energy pulses.

In this study, pulses were optimized to maximize the magnetization difference

between 2 samples. Note that it is possible to control more than 2 trajectories in order to optimize the contrast between several samples. This implies a cost function adaptation, but does not change the proposed formalism. An example of multiple trajectory control was shown in [26].
In vivo feasibility of the control of MRI contrast with RF pulses has been demonstrated in this work, but the proposed approach needs further developments to be applied routinely. In particular, the acquisition time should be competitive with standard acquisitions for different encoding schemes (spin-echo or gradient-echo). RARE factors are used in this study to accelerate spin-echo acquisitions, but the current implementation does not allow TR shortening or flip angle reduction as used for example in FLASH sequences. Future work will thus concentrate on including temporal parameters into the optimization problem to improve the contrast-to-noise ratio (CNR) per unit of time [38]. Several aspects could be investigated in that regard: i) optimization of steady-state sequences to avoid the use of long TR waiting for complete longitudinal magnetization recovery, ii) development of new cost functions that balance the contrast with the amount of acquired signal to optimize the CNR, iii) the numerical resolution of contrast time-minimal problems following the works of [29, 39].

7. Conclusion

This paper details the theoretical and practical benefits of using optimal control pulses to generate contrast in MRI. Optimal pulses are generated with a gradient-descent based algorithm which has proved to be robust to a wide range of experimental variations. Simulation results quantify the theoretical contrast improvement compared to standard contrast strategies. In particular, they suggest that T_2 differences can be used in order to maximize the signal coming from short T_2 samples. Their use in MRI is validated through both *in vitro* and *in vivo* experiments, and their integration into standard imaging sequences as preparation pulses is detailed. *In vitro* experiments show that in practice, standard contrasts can be improved using optimal contrast pulses. *In vivo* experiments on mouse and rat brains are performed to validate the ability of optimal pulses to maximize short T_2 tissues. A non-trivial contrast between white and gray matter is obtained, which could potentially be useful for an optimal discrimination of these two tissues. Other practical applications could be to have insights on the best achievable contrast for given sample characteristics together with the RF

pulse that produces such contrast, and perhaps reduce the use of invasive and costly contrast agents.

Acknowledgements

This work is supported by the ANR-DFG research program Explosys (Grant No. ANR-14-CE35-0013-01; GL203/9-1) and from the Technische Universität München Institute for Advanced Study, funded by the German Excellence Initiative and the E. U. Seventh Framework Programme under Grant No. 291763. This work was performed within the framework of the LABEX PRIMES (ANR-11-LABX-0063/ ANR-11-IDEX-0007).

[1] E. M. Haacke, R. W. Brown, M. R. Thompson, R. Venkatesan *et al.*, *Magnetic resonance imaging: physical principles and sequence design*. Wiley-Liss New York, 1999, vol. 82.

[2] S. Conolly, D. Nishimura, and A. Macovski, "Optimal control solutions to the magnetic resonance selective excitation problem," *IEEE transactions on medical imaging*, vol. 5, no. 2, pp. 106–115, 1986.

[3] T. E. Skinner, T. O. Reiss, B. Luy, N. Khaneja, and S. J. Glaser, "Application of optimal control theory to the design of broadband excitation pulses for high-resolution {NMR}," *Journal of Magnetic Resonance*, vol. 163, no. 1, pp. 8 – 15, 2003. [Online]. Available: http://www.sciencedirect.com/science/article/pii/S1090780703001538

[4] H. Liu and G. B. Matson, "Radiofrequency pulse designs for three-dimensional mri providing uniform tipping in inhomogeneous b1 fields," *Magnetic resonance in medicine*, vol. 66, no. 5, pp. 1254–1266, 2011.

[5] M. A. Janich, R. F. Schulte, M. Schwaiger, and S. J. Glaser, "Robust slice-selective broadband refocusing pulses," *Journal of Magnetic Resonance*, vol. 213, no. 1, pp. 126–135, 2011.

[6] M. A. Janich, M. A. McLean, R. Noeske, S. J. Glaser, and R. F. Schulte, "Slice-selective broadband refocusing pulses for the robust generation of crushed spin-echoes," *Journal of Magnetic Resonance*, vol. 223, pp. 129–137, 2012.

[7] K. Kobzar, S. Ehni, T. E. Skinner, S. J. Glaser, and B. Luy, "Exploring the limits of broadband 90° and 180° universal rotation pulses." *Journal of Magnetic Resonance*, vol. 225, pp. 142 – 160, 2012. [Online]. Available: http://search.ebscohost.com.gate6.inist.fr/login.aspx?direct=true&db=edselp&AN=S1090780712003126&lang=fr&site=eds-live

[8] T. E. Skinner, N. I. Gershenzon, M. Nimbalkar, and S. J. Glaser, "Optimal control design of band-selective excitation pulses that accommodate relaxation and rf inhomogeneity." *Journal of Magnetic Resonance*, vol. 217, pp. 53 – 60, 2012. [Online]. Available: http://search.ebscohost.com.gate6.inist.fr/login.aspx?direct=true&db=edselp&AN=S109078071200064X&lang=fr&site=eds-live

[9] T. E. Skinner, N. I. Gershenzon, M. Nimbalkar, W. Bermel, B. Luy, and S. J. Glaser, "New strategies for designing robust universal rotation pulses: application to broadband refocusing at low power," *Journal of Magnetic Resonance*, vol. 216, pp. 78–87, 2012.

[10] M. S. Vinding, I. I. Maximov, Z. Tošner, and N. C. Nielsen, "Fast numerical design of spatial-selective rf pulses in mri using krotov and quasi-newton based optimal control methods," *The Journal of Chemical Physics*, vol. 137, no. 5, 2012. [Online]. Available: http://scitation.aip.org/content/aip/journal/jcp/137/5/10.1063/1.4739755

[11] I. I. Maximov, M. S. Vinding, H. Desmond, N. C. Nielsen, and N. J. Shah, "Real-time 2d spatially selective mri experiments: Comparative analysis of optimal control design methods," *Journal of magnetic resonance*, vol. 254, pp. 110–120, 2015.

[12] C. S. Aigner, C. Clason, A. Rund, and R. Stollberger, "Efficient high-resolution rf pulse design applied to simultaneous multi-slice excitation," *Journal of Magnetic Resonance*, vol. 263, pp. 33–44, 2016.

[13] D. Xu, K. F. King, Y. Zhu, G. C. McKinnon, and Z.-P. Liang, "Designing multichannel, multidimensional, arbitrary flip angle rf pulses using an optimal control approach," *Magnetic resonance in medicine*, vol. 59, no. 3, pp. 547–560, 2008.

[14] W. A. Grissom, D. Xu, A. B. Kerr, J. A. Fessler, and D. C. Noll, "Fast large-tip-angle multidimensional and parallel rf pulse design in mri,"

IEEE transactions on medical imaging, vol. 28, no. 10, pp. 1548–1559, 2009.

[15] A. Massire, M. A. Cloos, A. Vignaud, D. L. Bihan, A. Amadon, and N. Boulant, "Design of non-selective refocusing pulses with phase-free rotation axis by gradient ascent pulse engineering algorithm in parallel transmission at 7 t," *Journal of Magnetic Resonance*, vol. 230, pp. 76 – 83, 2013. [Online]. Available: http://www.sciencedirect.com/science/article/pii/S1090780713000190

[16] A. Sbrizzi, H. Hoogduin, J. V. Hajnal, C. A. van den Berg, P. R. Luijten, and S. J. Malik, "Optimal control design of turbo spin-echo sequences with applications to parallel-transmit systems," *Magnetic resonance in medicine*, 2016.

[17] V. Gras, A. Vignaud, A. Amadon, F. Mauconduit, D. Bihan, and N. Boulant, "In vivo demonstration of whole-brain multislice multispoke parallel transmit radiofrequency pulse design in the small and large flip angle regimes at 7 tesla," *Magnetic Resonance in Medicine*, 2016.

[18] M. S. Vinding, D. Brenner, D. H. Y. Tse, S. Vellmer, T. Vosegaard, D. Suter, T. Stöcker, and I. I. Maximov, "Application of the limited-memory quasi-newton algorithm for multi-dimensional, large flip-angle rf pulses at 7t," *Magnetic Resonance Materials in Physics, Biology and Medicine*, vol. 30, no. 1, pp. 29–39, 2017. [Online]. Available: http://dx.doi.org/10.1007/s10334-016-0580-1

[19] V. Gras, A. Vignaud, A. Amadon, D. Le Bihan, and N. Boulant, "Universal pulses: A new concept for calibration-free parallel transmission," *Magnetic Resonance in Medicine*, vol. 77, no. 2, pp. 635–643, 2017. [Online]. Available: http://dx.doi.org/10.1002/mrm.26148

[20] B. Bonnard, O. Cots, S. Glaser, M. Lapert, D. Sugny, and Y. Zhang, "Geometric optimal control of the contrast imaging problem in nuclear magnetic resonance," *IEEE Transactions on Automatic Control*, vol. 57, no. 8, pp. 1957–1969, 2012.

[21] M. Lapert, Y. Zhang, M. Janich, S. Glaser, and D. Sugny, "Exploring the physical limits of saturation contrast in magnetic resonance imaging," *Scientific Reports*, vol. 2, no. 589, 2012.

[22] E. Assémat, M. Lapert, D. Sugny, and S. J. Glaser, "On the application of geometric optimal control theory to nuclear magnetic resonance," *Mathematical Control And Related Fields*, vol. 3, no. 4, pp. 375–396, 2013.

[23] B. Bonnard, M. Claeys, O. Cots, and P. Martinon, "Geometric and numerical methods in the contrast imaging problem in nuclear magnetic resonance," *Acta Applicandae Mathematicae*, vol. 135, no. 1, pp. 5–45, 2014.

[24] B. Bonnard and O. Cots, "Geometric numerical methods and results in the contrast imaging problem in nuclear magnetic resonance," *Mathematical Models and Methods in Applied Sciences*, vol. 24, no. 01, pp. 187–212, 2014.

[25] Y. Chang, D. Wei, S. J. Glaser, and X. Yang, "Optimized phase-sensitive inversion recovery for mri contrast manipulation," *Applied Magnetic Resonance*, vol. 46, no. 2, pp. 203–217, 2015. [Online]. Available: http://dx.doi.org/10.1007/s00723-014-0629-0

[26] E. Van Reeth, H. Ratiney, M. Tesch, S. J. Glaser, and D. Sugny, "Optimizing mri contrast with b1 pulses using optimal control theory," in *IEEE 12th International Symposium on Biomedical Imaging (ISBI)*. IEEE, 2016.

[27] J. S. Glaser, U. Boscain, T. Calarco, P. C. Koch, W. Köckenberger, R. Kosloff, I. Kuprov, B. Luy, S. Schirmer, T. Schulte-Herbrüggen, D. Sugny, and K. F. Wilhelm, "Training schrödinger's cat: quantum optimal control," *The European Physical Journal D*, vol. 69, no. 279, pp. 1–24, 2015. [Online]. Available: http://dx.doi.org/10.1140/epjd/e2015-60464-1

[28] L. S. Pontryagin, *Mathematical theory of optimal processes*. CRC Press, 1987.

[29] B. Bonnard, M. Chyba, and J. Marriott, "Singular trajectories and the contrast imaging problem in nuclear magnetic resonance," *SIAM Journal on Control and Optimization*, vol. 51, no. 2, pp. 1325–1349, 2013.

[30] N. Khaneja, T. Reiss, C. Kehlet, T. Schulte-Herbrüggen, and S. J. Glaser, "Optimal control of coupled spin dynamics: design of nmr

pulse sequences by gradient ascent algorithms," *Journal of Magnetic Resonance*, vol. 172, no. 2, pp. 296 – 305, 2005. [Online]. Available: http://www.sciencedirect.com/science/article/pii/S1090780704003696

[31] M. Lapert, "On grape implementation," April 2015, private note.

[32] W. Squire and G. Trapp, "Using complex variables to estimate derivatives of real functions," *Siam Review*, vol. 40, no. 1, pp. 110–112, 1998.

[33] I. I. Maximov, J. Salomon, G. Turinici, and N. C. Nielsen, "A smoothing monotonic convergent optimal control algorithm for nuclear magnetic resonance pulse sequence design," *The Journal of chemical physics*, vol. 132, no. 8, p. 084107, 2010.

[34] P. de Fouquieres, S. Schirmer, S. Glaser, and I. Kuprov, "Second order gradient ascent pulse engineering," *Journal of Magnetic Resonance*, vol. 212, no. 2, pp. 412 – 417, 2011. [Online]. Available: http://www.sciencedirect.com/science/article/pii/S1090780711002552

[35] J. Hennig, A. Nauerth, and H. Friedburg, "Rare imaging: a fast imaging method for clinical mr," *Magnetic resonance in medicine*, vol. 3, no. 6, pp. 823–833, 1986.

[36] R. A. de Graaf, P. B. Brown, S. McIntyre, T. W. Nixon, K. L. Behar, and D. L. Rothman, "High magnetic field water and metabolite proton t1 and t2 relaxation in rat brain in vivo," *Magnetic resonance in medicine*, vol. 56, no. 2, pp. 386–394, 2006.

[37] S. Black, F. Gao, and J. Bilbao, "Understanding white matter disease," *Stroke*, vol. 40, no. 3 suppl 1, pp. S48–S52, 2009.

[38] M. Lapert, E. Assémat, S. Glaser, and D. Sugny, "Optimal control of the signal-to-noise ratio per unit time for a spin-1/2 particle," *Physical Review A*, vol. 90, no. 2, p. 023411, 2014.

[39] M. Lapert, Y. Zhang, S. Glaser, and D. Sugny, "Towards the time-optimal control of dissipative spin-1/2 particles in nuclear magnetic resonance," *Journal of Physics B: Atomic, Molecular and Optical Physics*, vol. 44, no. 15, p. 154014, 2011.